Atrazine adsorption by graphene-based materials: Interaction mechanism and application in real samples

Caihong Cheng [a,b,1], Xuejuan Shi [c,1], Gengwen Yin [d], Fei Peng [a,b],
Wenlong Hou [a,b], Weiguo Zhang [a], Xiaohu Lin [a], Jun Li [e,*], Xiuping Wang [a,c,**]

[a] Analysis and Testing Center, Hebei Normal University of Science and Technology, Qinhuangdao 066000, PR China
[b] Hebei Key Laboratory of Active Components and Functions in Natural Products, Hebei Normal University of Science and Technology, Qinhuangdao, 066004, PR China
[c] Hebei Key Laboratory of Crop Stress Biology (in preparation), College of Agronomy and Biotechnology, Hebei Normal University of Science and Technology, Qinhuangdao 066000, PR China
[d] Library, Hebei Normal University of Science and Technology, Qinhuangdao 066000, PR China
[e] Oil Crops Research Institute, Chinese Academy of Agricultural Sciences, Wuhan 430070, PR China

ARTICLE INFO

ABSTRACT

The wide use of atrazine (ATZ) as a triazine herbicide poses serious threats to the environment and human health. Therefore, it is particularly necessary to develop some effective methods for the removal of ATZ from the environment. Here, we studied the removal of ATZ from aqueous solutions by three graphene-based materials (GBMs), including graphene oxide (GO), reduced graphene oxide (rGO) and graphene nanoplatelets (GNP). The results revealed that all the three GBMs had extremely high ATZ adsorption capacity, which followed the order of rGO (1083.94 mg/g) > GO (1011.94 mg/g) > GNP (1005.77 mg/g), and they were also confirmed to be applicable to actual samples. The adsorption was well fitted by the Elovich kinetic model with the determination coefficient (R^2) > 0.985, 0.998 and 0.993 for GO, rGO and GNP, respectively. Moreover, the adsorption isotherm data were fitted to the Langmuir, Freundlich, Temkin, Dubinin–Radushkevich and Sips models. The results revealed that the adsorption process was the best fit by the Sips model. The fitting results of adsorption kinetics and adsorption isotherm demonstrated that the adsorption is a multi-mechanism process. In addition, the interaction mechanism of ATZ with the adsorbents was investigated by density functional theory (DFT), and the visual illustration revealed that the adsorption process was driven synergistically by H-bonding and $\pi - \pi$ conjugation interactions. The developed materials are of high convenience and feasibility, and have great application potential in the removal of ATZ and other pesticides from the aqueous environment.

© 2022 The Author(s). Published by Elsevier B.V. This is an open access article under the CC BY-NC-ND license (http://creativecommons.org/licenses/by-nc-nd/4.0/).

1. Introduction

Over the past decades, herbicides have been widely used in agricultural and aquacultural practices to remove field weeds or as environmental modifiers to remove harmful algae, weeds and moss in water bodies (Hamilton et al., 2011;

---

* Corresponding author.
** Correspondence to: Analysis and Testing Center, Hebei Normal University of Science and Technology, No.360 west section of Hebei street, Qinhuangdao 066000, Hebei Provence, PR China.
   E-mail addresses: lijun02@caas.cn (J. Li), wangxiuping0721@163.com (X. Wang).
[1] Caihong Cheng and Xuejuan Shi contributed equally to this work.

Souza et al., 2020). Large amounts of herbicides have entered the environment in various forms and eventually pollute the soil and water bodies, posing serious threats to humans and the environment (Yang et al., 2019; Yu et al., 2021). Among herbicides, atrazine (ATZ; chemical structure shown in **Fig. S1**) is widely used and becomes a particularly ubiquitous micropollutant (He et al., 2019). Due to its selectivity and high water solubility, ATZ is used both as a pre-emergent and early post-emergent herbicide. This herbicide is widely used to control dicotyledonous weeds and some grasses in agriculture in order to improve the yield of crops (Khavar et al., 2018; Li et al., 2018). However, due to the long half-life and large application amount, ATZ residues are gradually accumulated as environmental pollutants in water bodies and pose potential hazards to the environmental and human health (Dionne et al., 2021; Vieira et al., 2021). Therefore, it is urgent to develop effective methods for the removal of ATZ residues from the environment.

In recent years, many remediation techniques have been developed to reduce the harm caused by ATZ, such as Fenton reaction (Yang et al., 2018; Fareed et al., 2021), ozonation (Yuan et al., 2019), adsorption (Wang et al., 2020; Ighalo et al., 2020; Adeniyi et al., 2021; Binh et al., 2022), and chlorination methods (Kong et al., 2016). Among these methods, adsorption has been recognized as a superior and widely used method owing to its relatively low cost, easy operation and eco-friendly water cleaning effect. Currently, carbon-based nanomaterials have been developed as high-performance adsorbents to be widely used in the adsorption of heavy metal ions, dyes and other pollutants from aqueous solutions, due to their high stability, large specific surface area, rich sp^2 bonds, abundant oxygen functional groups and large $\pi-\pi$ conjugated structure (Bhattacharyya et al., 2021; Mehrabi et al., 2019; Velásquez-Rojas et al., 2021; Al-Ghouti et al., 2022). For instance, Kuang et al. (2020) reported the adsorption of methylene blue by activated carbon (AC) modified with anionic surfactant (SLS), which exhibited a high adsorption capacity of 232.5 mg/g. In addition, the adsorption of Cd^{2+} by nonmagnetic and magnetic biochars (CMB and M-CMB) was conducted in a previous study, and the maximum adsorption capacity could reach 60.69 and 41.07 mg/g at the initial Cd^{2+} concentration of 180 mg/L, respectively (Huang et al., 2020).

Compared with other carbonaceous materials, graphene-based materials (GBMs) such as graphene oxide (GO), reduced graphene oxide (rGO) and graphene nanoplatelets (GNP) have the advantage of selective adsorption for organic pollutants through strong $\pi-\pi$ interaction, electrostatic interaction and H-bonding interaction (Molla et al., 2019; Nithya Priya et al., 2022; Zarenezhad et al., 2022). For instance, Zhao et al. (2019) investigated the adsorption performance of tetracycline–Cu multi-pollutants by GO and rGO, and concluded that the adsorption mechanism mainly includes $\pi-\pi$ conjugation, electrostatic interaction, and the bridge connection by Cu^{2+}. Moreover, commercial GNP could remove tetracycline antibiotics from aqueous solutions with an adsorption capacity up to 240.4 mg/g when used as an adsorbent (Sui et al., 2017). Although there have been numerous studies of the adsorption behavior of GBMs, there were relatively few studies of GBMs to be used for herbicide removal. In this work, ATZ was selected as the representative pesticide pollutant, and GO, rGO and GNP were used as adsorbents for the removal of ATZ from aqueous solutions and studying the adsorption behavior. The main objective is to ascertain the adsorption capacity of GO, rGO and GNP for ATZ and investigate the interaction mechanism between them. Finally, the applicability and of GBMs as adsorbents for real samples was tested. The results may provide valuable information for the removal of pesticides from aqueous environments using GBMs.
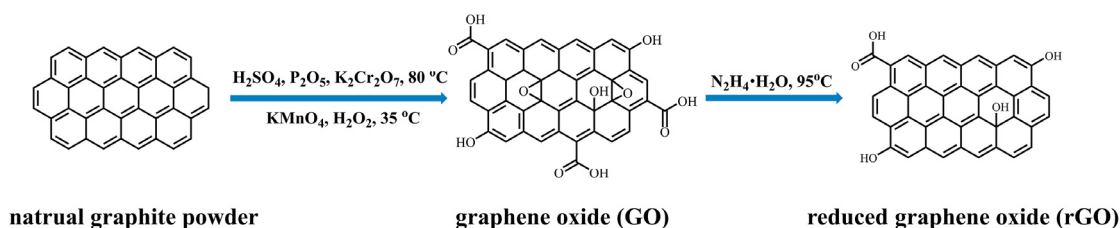
2. Experimental

2.1. Materials

GNPs were obtained from Sigma-Aldrich Co. Inc., and the analytical-grade chemicals needed for GO and rGO synthesis such as potassium permanganate ($KMnO_4$) and H_2O_2 were supplied by Merck Ltd., India. Concentrated sulfuric acid (H_2SO_4) and hydrochloric acid (HCl) were provided by Tianjin No. 3 Chemical Plant. Hydrazine hydrate ($NH_2NH_2 \cdot H_2O$) was obtained from Tokyo Chemical Industry Co. Ltd. ATZ (99.3%) was purchased from Beijing North Weiye Measurement Technology Research Institute (Beijing, China).

2.2. Preparation and characterization of GBMs

A modified Hummers' method described in our previous study was used to prepare GO. Typically, natural graphite powder was initially oxidized by H_2SO_4 to form graphite oxide (GtO). After filtration and washing with hydrochloric acid (10% V/V) and deionized water (DI) to remove the chemical residues, the GtO sample dispersed in deionized water was subjected to ultrasonic treatment (Elamsonic, S60 H) for 1 h and then centrifuged at 5000 rpm for 15 min to remove the unexfoliated GtO (Wang et al., 2018). Dried GO (100 mg) was dispersed in ultra-pure water (100 mL) under strong stirring and ultrasonication for at least 1 h. The sample was reduced with hydrazine hydrate (hydrazine hydrate/GO = 10, w/w) at 95 °C stirring for 8 h to obtain rGO. Then, the obtained rGO powder was filtered, and washed with ultra-pure water (5 × 100 mL) and methanol (5 × 100 mL), and finally dried at 40 °C for 24 h to remove residual solvent. The detail process for synthesizing GO and rGO is shown in Scheme 1.

The thermal stability and composition of the samples were tested with the thermal gravimetric analysis (TGA) (STA 409 PC Luxx, NETZSCH, Germany) at the rate of 10 °C/min in a N_2 atmosphere, and the temperature range was set from 20 °C to 700 °C. Fourier Transform Infrared Spectroscopy (FTIR) (TENSOR 27, Brucker, Germany) was used to analyze the functional groups and chemical bond types of samples in the range of 500–4000 cm^{-1}. The Raman spectrometer used in

Scheme 1. The synthesis process of GO and rGO.

Table 1
Porous properties of GBMs.

Properties	GO	rGO	GNP
BET Surface area (m^2/g)	246.31	357.56	26.52
BJH pore volume (cm^3/g)	1.60	0.35	0.18
Pore size (nm)	26.00	3.94	26.70

this experiment was the Scientific LabRAM HR Evolution microscopic confocal Raman spectrometer of HORIBA, with an excitation source of 633 nm and a Si detector. The structure and surface morphology of the sample were examined by field emission scanning electron microscope (FE-SEM) (SU8010, Hitachi, Japan). The surface elemental composition of GO, rGO and GNP was quantified using the X-ray photoelectron spectrometer (XPS) (AXIS Supra, SHIMADU, Japan). The BET surface, Pore volume and pore size of GBMs determined by a surface area analyzer (BSD-PM1, Beijing, China) are shown in Table 1.

2.3. Adsorption kinetic and isotherm studies

All the adsorption kinetics and adsorption isothermal experimental data were calculated by SPSS statistical software, and the model curve was fit and plotted by Origin 9.0.

2.3.1. Batch adsorption experiments

A series of adsorption kinetic experiments of ATZ by three GBMs (GO, rGO and GNP) were carried out. GO, rGO and GNP (1 mg for each) were respectively dispersed in 20 mL ultra-pure water mixed with ATZ at the concentration of 100 mg/L in a 50-mL centrifuge tube. The centrifuge tube was then placed on a laboratory shaking table (Orbital ShakerIncubator ES-20, Grant-Bio) at 22 °C. Then, the sample was taken at the scheduled time points (0.25, 0.50, 1.00, 1.50, 2.00, 2.50, 3.00, 4.00, 5.00, 6.00, 7.00, 8.00, 9.00 h), centrifuged for 1 min at 14 000 rpm, and the supernatant was filtered through a 0.45 μm polyethersulfone filter (Agela Technologies, Tianjin, China) attached to a syringe. The concentration of ATZ in the filtered solution was then determined by high performance liquid chromatography (HPLC) analysis.

The adsorption isotherm experiments were carried out with the same procedures used for the adsorption kinetic experiments, and the concentration of the ATZ solution was set from 6.25 to 150 mg/L. All experiments were carried out in triplicate, and the results were expressed as the average. A blank test was carried out under the same conditions without the use of any adsorbent. The initial and equilibrium concentrations of ATZ were used to calculate the adsorption capacity (mg/g). The adsorption amount of ATZ on each adsorbent was calculated as follows:

$$q_t = \frac{(C_0 - C_e)V}{m}, \tag{1}$$

where q_t is the adsorption amount of ATZ by per kilogram of absorbent (mg/g) at time t, V represents the volume (L) of the sample, C_e indicates the equilibrium concentration of ATZ (mg/L), C_0 represents the initial ATZ concentration (mg/L), and m represents the mass of the absorbent (g).

2.3.2. Adsorption kinetic models

Kinetic models can be used to ascertain the relationship between adsorption time and adsorption capacity to analyze the adsorption mechanism (Li et al., 2021). The pseudo first-order kinetic model is usually used to describe the initial stage of adsorption controlled by the diffusion step and cannot be used to accurately describe the whole adsorption process. However, the pseudo second-order kinetic model is based on the assumption that the adsorption rate is controlled by the chemical adsorption mechanism, which can be used to accurately describe the whole process of adsorption. The Elovich model is often used to describe heterogeneous adsorption process. Here, the three kinetic experimental models (pseudo first-order, pseudo second-order, and Elovich) were adopted for kinetic data fitting of the adsorption of GO, rGO and GNP for ATZ:

$$q_t = q_e(1 - e^{-k_1 t}) \tag{2}$$

$$q_t = \frac{q_e^2 k_2 t}{1 + k_2 q_e t} \tag{3}$$

$$q_t = \frac{1}{\beta} \ln(1 + \alpha\beta t) \tag{4}$$

Eqs. (2)–(4) are the pseudo first-order, pseudo second-order and Elovich kinetic experimental models, respectively, where q_e (mg/g) and q_t (mg/g) are the amounts of adsorbate adsorbed at equilibrium and time t (h), respectively; k_1 and k_2 stand for the first-order and second-order adsorption rate constants (1/h), respectively; α is the initial adsorption rate (mg/kg), and β is the desorption constant (kg/mg).

2.3.3. Adsorption isotherm models

To analyze the adsorption mechanism of GO, rGO and GNP for ATZ, the Langmuir, Freundlich, Temkin, Dubinin–Radushkevich and Sips isotherm models were used to test the experimental data. Langmuir isotherm assumes that the energy sites on the adsorbent surface are uniform, and the Langmuir equation (Saxena et al., 2019) is shown as follows Eq. (5):

$$q_e = \frac{Q_{max}^0 K_L C_e}{1 + K_L C_e}, \tag{5}$$

where Q_{max}^o (mg/g) is the maximum saturated monolayer adsorption capacity of an adsorbent, C_e (mg/L) represents the adsorbate concentration at equilibrium, q_e (mg/g) is the amount of adsorbate at equilibrium, and K_L (L/mg) is the affinity constant between the adsorbent and adsorbate. The nonlinearity of the Freundlich isotherm model (Banisheykholeslami et al., 2021) is shown in Eq. (6):

$$q_e = K_F C_e^n, \tag{6}$$

where K_F (mg/g)/(mg/L)^n is the Freundlich constant, and n is the Freundlich intensity parameter, which indicates the magnitude of the adsorption driving force or the surface heterogeneity. The Temkin isotherm model (Kesarwani et al., 2021) can be expressed by Eq. (7) and the Dubinin–Radushkevich isotherm models (Isiuku et al., 2021; Srivastava et al., 2017) can be shown as Eqs. (8)–(10):

$$q_e = \frac{RT}{b_T} \ln A_T C_e \tag{7}$$

$$Q_e = q_{DR} e^{-K_{DR}\varepsilon^2} \tag{8}$$

$$\varepsilon = RTLn\left[1 + \frac{1}{C_e}\right] (9) \tag{9}$$

$$E = 1/\sqrt{2K_{DR}} \tag{10}$$

In these equations, the constant A_T (L/mg) is the Temkin constant and b_T (kJ/moL) is the heat constant of adsorption; T (in Kelvin) is the temperature; R (8.314 J/mol/K) is the universal gas constant and ε is the Polanyi potential; q_{DR} is the theoretical adsorption capacity (mg/g); K_{DR} indicates a constant related to the absorption energy (mol^2/kJ^2); E is the mean free energy of adsorption (kJ/moL). In the Sips Eq. (11) (Wanjeria et al., 2018), Ks (L/mg) is the Sips model isotherm constant; a_s (L/mg) is the Sips model constant; and b_s is the Sips model exponent.

$$q_e = \frac{K_s C_e^{b_s}}{1 + a_s C_e^{b_s}} \tag{11}$$

2.4. HPLC analysis

The treated solution of ATZ was analyzed by a HPLC system (Diane UltiMate_3000, Thermofisher, USA) equipped with a UV detector. An Agilent ZORBAX Eclipse XDB-C18 column with the size of 5.0 μm, 150 mm × 4.6 mm was used for chromatographic fractionation. By using 70% methanol +30% water (V/V) as the mobile phase, the ATZ solution was separated by isocratic elution in 10 min with the detection wavelength of 225 nm. The flow rate was 0.8 mL/min, and the injection volume was 10 μL. Under these conditions, the retention time of ATZ was 4.66 ± 0.02 min.

2.5. Interaction mechanism determined by theoretical calculation

In order to fully investigate the interaction mechanism between the adsorbate and adsorbents, DFT was employed to study the optimized geometry and binding energies (BEs) between the adsorbent and ATZ. The initial geometry optimization was carried out using B3LYP-D3(BJ) functional (Grimme et al., 2011) in conjunction with 6-311G (d, p) basis set (Mclean and Chandler, 1980) in vacuum. All the structures were confirmed to be in local minima via vibrational frequency calculation. The independent gradient model based on Hirshfeld partition (IGMH) analyses was performed
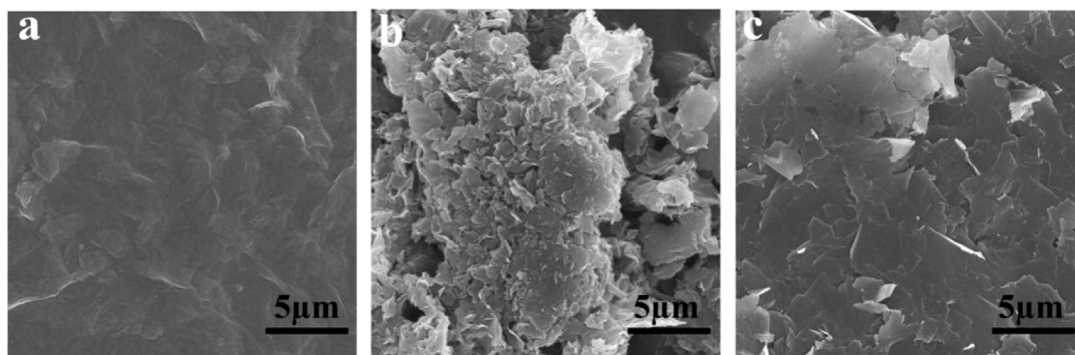
Fig. 1. FE-SEM images of GO (a), rGO (b) and GNP (c).

via the Multiwfn 3.8(*dev*) code (Lu and Chen, 2012, 2021). To represent the typical functional domains of GBMs, a 19-membered carbon ring was used as the model structure for the sp^2 region of GBMs, and the 19-membered carbon ring with three hydroxyl groups, one epoxide group and one carboxyl group was used as the sp^3 region model structure of GBMs in this study. The BEs were calculated at M06-2X-D3 (Zhao et al., 2006)/6-311+G (*d, p*) level by a correction of basis set superposition error (BSSE) through the following Eq. (12):

$$BE = E_{\text{GBMs(sp2/sp3)}-\text{ATZ}} - E_{\text{GBMs(sp2/sp3)}} - E_{\text{ATZ}} \qquad (12)$$

2.6. Real samples

To confirm the applicability of the adsorbents in actual samples, the adsorption of ATZ in spiked tap water and wastewater samples was conducted with the tested absorbents. The adsorbent dose was set as 1 mg while the ATZ concentration was set as 100 mg/L. The experiments were carried out as described in the adsorption experiment and the HPLC analysis method was employed to confirm the concentration of ATZ. The parameters of tap water and waste water are presented in **Table S1**.

2.7. Reutilization test

After the adsorption test, the adsorbent was collected by centrifugation, and then eluted with chromatographic pure dichloromethane, and separated by a separating funnel. The elution was repeated for four times. The eluent was determined by HPLC until the eluent contained no ATZ. The eluted adsorbent was dried in an oven at 40 °C and reused as an adsorbent for adsorption. About 1 mg of recovered adsorbent was accurately weighed into a 50 mL centrifuge tube, which was then added with 20 mL of 100 mg/L ATZ solution. Three parallel samples were set for all experimental samples. The samples were placed in a laboratory shaking table with an oscillation frequency of 200 rpm at 22 °C for 9 h. After centrifugation at 14 000 r/min for 1 min, the supernatant was filtered by 0.45 μm polyethersulfone filter and stored in the liquid chromatography injection bottle. The residual amount of ATZ was determined by HPLC. In this way, the re-adsorption experiments were performed for three times using the recovered adsorbents.

3. Results and discussion

3.1. Characterization of the adsorbents

The BET surface area of GBMs was characterized by a surface area analyzer and shown in Table 1. The values of the BET surface area for GO, rGO and GNP were 246.31, 357.56 and 26.52 m^2/g, respectively. Further, the FE-SEM, TGA, XPS and Raman spectra of GBMs were characterized and the FE-SEM images display their microstructures. As shown in Fig. 1, GO exhibited a significantly different surface morphology from rGO and GNP. Fig. 1a shows that the surface of GO was thin and smooth, consisting of partially folded structures, which could result in multilayer aggregation due to the presence of oxygen-containing groups. These results indicate that GO has been well exfoliated and prepared. However, the surface of rGO was rough with more folds and some disorganized flakes (Fig. 1b), which might reduce the polymerization and provide a large available specific surface area to facilitate the adsorption (Zhao et al., 2019). Fig. 1c shows that the GNP surface consisted of a stack of flat-structured sheets, which might interact with the adsorbate mainly through the π–π stacking interaction for adsorption and therefore be more conducive to the adsorption of pollutants containing aromatic structure.

To verify the chemical structure of GO, rGO and GNP, the Raman spectra were obtained and presented in Fig. 2a. The Raman spectrum of GNP showed a peak at 1583 cm^{-1}, which is a G-band. The Raman spectra of GO showed two peaks
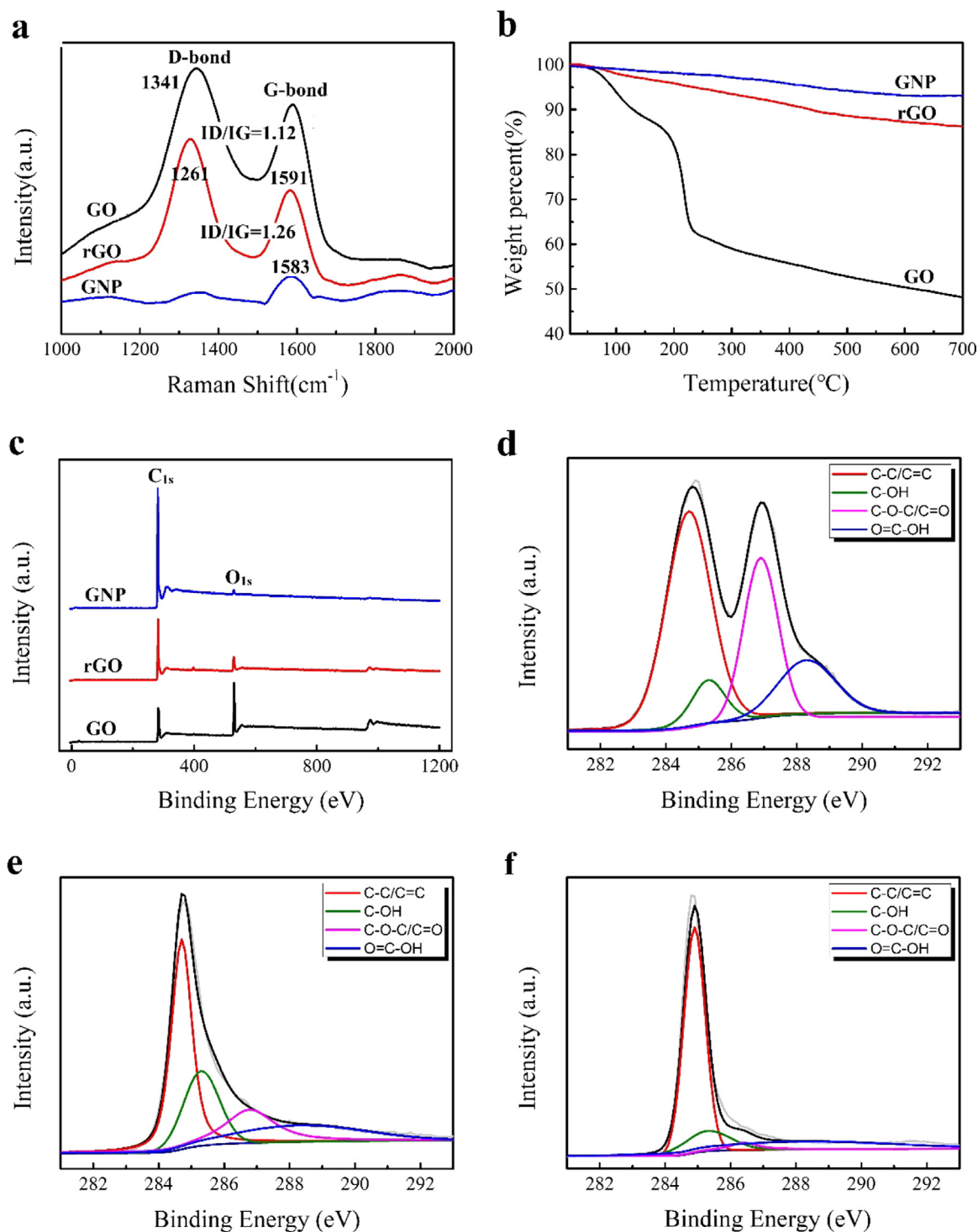
Fig. 2. Characterization of GBMs. Raman spectra (a), ID is the intensity of D-bond, IG is the intensity of G-bond; TGA curves (b); XPS spectra (c). Deconvolution of the C 1s XPS peak of GO (d), rGO (e) and GNP (f).

of the D- and G-band at 1341 and 1591 cm^{-1}, respectively. The G-band showed a blue shift relative to that of graphite, which might be due to the strong oxidation of graphite. The Raman spectra of rGO also showed two peaks of the D- and G-band, but the positions were shifted to 1326 and 1583 cm^{-1}, respectively. The rGO had a higher intensity ratio of

Table 2

Analysis of C1s peaks and relative percentages of different functional groups obtained from XPS spectra.

Binding energy (eV)	Assignment	Relative fraction of each C moiety		
		GO	rGO	GNP
284.6	C–C/C=C	43.4%	47.7%	90.6%
285.3	C–OH	8.5%	24.1%	5.3%
286.4	C–O–C/C=O	30.0%	19.0%	4.1%
288.3	O=C–OH	18.1%	9.2%	0

GO: graphene oxide; rGO: reduced graphene oxide; GNP: graphene nanoplatelets.

D-band to G-band (ID/IG; 1.26) compared with GO (1.12), which may be ascribed to the increase in the average size of the sp^2 region after the reduction of GO (Wang et al., 2013).

The TGA was used to evaluate the oxygen-containing functional groups on the surface of GBMs and their thermal stability as shown in Fig. 2b. The weight loss process of GO could be mainly divided into three stages: in the first stage (before 150 °C), the weight loss was due to the evaporation of water adsorbed on the surface of GO; while in the second stage (150–230 °C), it was owing to the thermal decomposition of oxygen-containing groups such as epoxy groups, carbonyl groups and hydroxyl groups on the surface of GO, which resulted in a higher weight loss of 48.11%; the weight loss in the last stage might be attributed to the decomposition of the carbon lattice in GO. rGO (by 13.80%) and GNP (by 6.83%) showed significantly less weight loss at 150–400 °C, which was far lower than that of GO (48.11%), indicating higher thermal stability of rGO and GNP than GO.

In order to further distinguish the structure of GO, rGO and GNP, their chemical composition was determined by XPS (Fig. 2c). As a result, the C1s (285.0 eV) and O1s (532.0 eV) energy spectra with significant variations in the C/O ratio were observed among the studied adsorbents. As shown in **Table S2**, GO had a high oxygen concentration of 27.56%, while that of rGO and GNP was only 8.92% and 1.27%, respectively. The C/O ratio of GO was 2.63, indicating the presence of numerous oxygen-containing groups on the surface of GO, which may destroy the sp^2 region of graphite. The C/O ratio of rGO was 10.21, indicating that a part of oxygen-containing groups on GO surface disappeared during the reduction and the sp^2 region was restored. The high C/O ratio of GNP suggested that it contained almost no oxygen-containing groups, which is consistent with its high thermal stability in the TGA analysis.

In Fig. 2d–f, the splitting of the C1s peaks by de-convolution using four different components revealed that the four peaks were respectively attributed to aromatic or aliphatic carbon C–C/C=C (∼284.6 eV), C–OH (∼285.3 eV), C–O–C/C=O (∼286.4 eV) and O–C=O (∼288.3 eV) (Gao et al., 2018; Liu et al., 2015). As shown in Fig. 2d–f, in the XPS spectrum of GO, rGO and GNP, there was a dominant peak of sp^2 C=C at 284.6 eV, which corresponds to the graphitic structure. Several small peaks of C–OH at 285.3 eV and C–O–C/C=O at 286.4 eV are assigned to carbon atoms attached to different oxygen-containing moieties. Based on the XPS results, the C1s peaks and relative percentages of different functional groups on the surface of GO, rGO and GNP were obtained (Table 2). The results revealed that the concentration of C–C/C=C increased in the order of GO, rGO and GNP, indicating that the concentration of oxygen-containing groups on the surface of the GBMs is in reverse proportion to that of C–C/C=C. For the oxygen-containing groups, the concentration of C–O–C/C=O and COOH moieties was almost 50.0% on GO surface while about 30% on rGO surface, implying reduction of partial C–O–C/C=O and COOH moieties during the reduction of GO to rGO, which is in line with the increase in the concentration of C–OH groups (24.1%) and C–C/C=C (47.7%) in rGO.

3.2. Adsorption capacity of the adsorbents

To evaluate the adsorption capacity of GBMs for ATZ, batch adsorption experiments were implemented. Pre-experiments were carried out on the factors that might affect the adsorption capacity, such as the adsorbent dose, pH and ATZ concentration. The results revealed that pH has little effect on the adsorption performance of the adsorbent (**Fig. S3**). When the adsorbent dose was 1 mg, the adsorption effect was the best, and there was no obvious change with increasing adsorbent dose. With increasing concentration of ATZ, the adsorption capacity increased and finally reached saturation. The maximum adsorption capacities of ATZ on GO, rGO and GNP were 1011.94, 1083.94 and 1005.77 mg/g, respectively, indicating that all the three adsorbents have excellent adsorption performance, particularly rGO.

The adsorption capacity of ATZ on GBMs may be affected by the effective BET surface area, H-bonding and π–π stacking interaction (El-Kammah et al., 2022). As shown in Table 1, the BET surface area values of GO and rGO are much greater than that of GNP, indicating that GO and rGO should have higher adsorption capacity for ATZ; however, GNP also exhibited excellent adsorption performance, possibly because besides the effective BET surface area, the H-bonding and π–π stacking interaction between ATZ and GBMs are also key factors affecting the adsorption capacity of ATZ on GBMs. The detailed mechanism for the effect of H-bonding and π–π stacking interaction on the adsorption capacity of ATZ on GBMs would be further investigated in Section 3.5. In addition, a comparison of the adsorption capacities of various adsorbents for ATZ as previously reported is presented in Table 5. It can be seen that GBMs are superior to many other adsorbents for ATZ adsorption. This result might be attributed to the synergistic effect of H-bonding and π–π stacking interaction between GBMs and ATZ molecules.
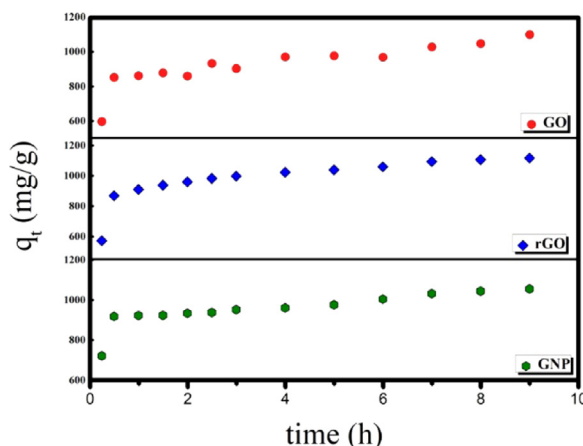
Fig. 3. Effects of contact time on the adsorption of ATZ onto GBMs.

Table 3
Fitting parameters of adsorption kinetics of ATZ onto GO, rGO and GNP with the pseudo first-order, pseudo second-order and Elovich kinetic models.

Materials	Pseudo-first order			Pseudo-second order			Elovich		
	q_e (mg/g)	k_1 (1/h)	R^2	q_e (mg/g)	k_2 (g/(mg h))	R^2	α (mg/g)	β (g/mg)	R_2
GO	961.38	3.8861	0.9347	1011.94	0.0067	0.9627	3.01×10^6	0.0123	0.9851
rGO	1028.59	3.2475	0.9590	1083.94	0.0055	0.9852	2.77×10^6	0.0114	0.9985
GNP	977.80	5.3543	0.9733	1005.77	0.0134	0.9835	3.35×10^9	0.0197	0.9938

3.3. Adsorption kinetics

Fig. 3 shows the changes in adsorption amount (q_t) of ATZ by GO, rGO and GNP with contact time. The absorption of ATZ by the three absorbents increased rapidly in the first 30 min and generally reached equilibrium within 1 h. To ensure that the adsorption of ATZ reached equilibrium, the adsorption time was set as 9 h. The commonly used pseudo first-order, pseudo second-order and Elovich kinetic models were used to fit the kinetic curve, respectively. The relevant fitting parameters and determination coefficients (R^2) are shown in Table 3. As a result, the Elovich kinetic model achieved better fitting than both the first-order kinetic model and second-order kinetic model, and the determination coefficients (R^2) were > 0.985, 0.998 and 0.993 for GO, rGO and GNP, respectively, indicating that the adsorption of ATZ by these three adsorbents involves multiple mechanisms.
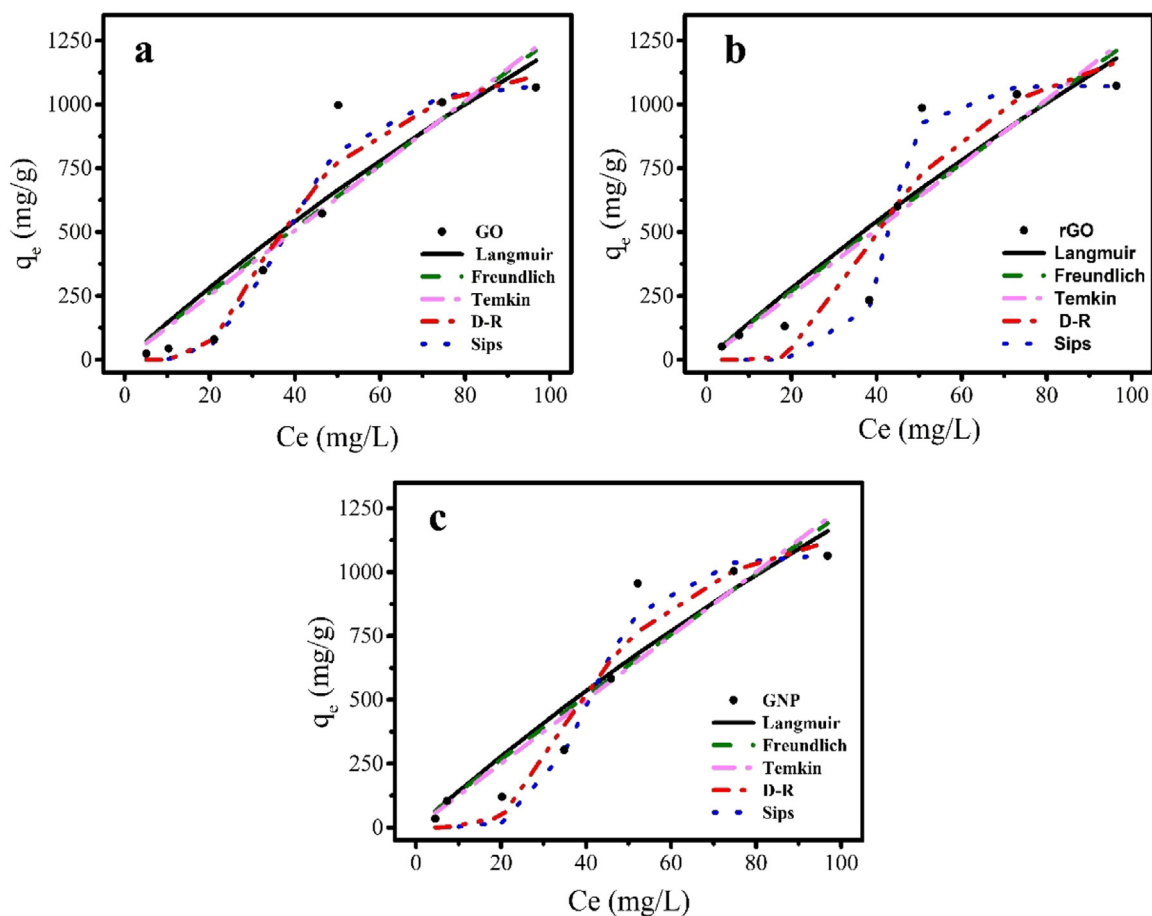
3.4. Adsorption isotherms

Adsorption isotherms are useful for investigating the relationship and interaction between the adsorbent and adsorbate when the adsorption process reaches equilibrium. To understand how the functional groups on GBMs affect the adsorption process, the adsorption isotherm curves of GO, rGO and GNP for ATZ were constructed (Nodeh et al., 2019; Wanjeria et al., 2018). The adsorption is a non-linear process as fitted by the Langmuir (Eq. (5), Freundlich (Eq. (6)), Temkin (Eq. (7)), Dubinin–Radushkevich (Eq. (8)) and Sips (Eq. (11)) adsorption models as shown in Fig. 4. The corresponding parameters are listed in Table 4. Compared with the Langmuir, Temkin and Freundlich models, the Dubinin–Radushkevich and Sips models, which are often used for heterogeneous adsorption processes, seemed to better fit the experimental data and describe the adsorption process of ATZ. Therefore, the adsorption process of ATZ by the three adsorbents should be multilayer heterogeneous adsorption, indicating that in the adsorption process, there are also some interactions between ATZ molecules besides the interaction between ATZ and the adsorbent.

As shown in Table 4, the Dubinin–Radushkevich isotherm model had a better fitting with the R^2 values above 0.9. The adsorption energy (E), which was used to estimate whether the adsorption process is chemisorption or physisorption, was 0.0485, 0.0421 and 0.0451 kJ/mol for GO, rGO and GNP, respectively, implying that the adsorption of ATZ on the three adsorbents is a physical adsorption process, and the adsorption process occurs on both homogeneous and heterogeneous surfaces (Tran et al., 2017; Wanjeria et al., 2018). This finding is consistent with the observation of FTIR analysis (**PS1 and Fig. S2**), which showed that the various functional groups of the adsorbent interacted with ATZ by the $\pi-\pi$ stacking and H-bonding interactions.

In general, the fitting of the Sips isotherm model was the most consistent with the experimental data. According to the graphical analysis (Fig. 4) and the corresponding data (Table 4), it can be used to well describe adsorption process of

Fig. 4. Experimental data fitting of ATZ adsorption by three adsorbents with various adsorption isothermal models: GO (a), rGO (b), GNP (c). (For interpretation of the references to colour in this figure legend, the reader is referred to the web version of this article.)

Table 4
Parameters of isotherm models for ATZ absorption.

Isotherm model	Isotherm parameter	GO	rGO	GNP
Langmuir	Q^0_{max} (mg/g)	6460.05	7197.21	6558.12
	K_L (L/mg)	0.0023	0.0020	0.0022
	R^2	0.8804	0.8504	0.8968
Freundlich	K_F (mg/g)/(mg/L)^n	14.52	15.36	15.45
	n	0.9678	0.9560	0.9503
	R^2	0.8656	0.8436	0.8883
Temkin	b (kJ/mol)	0.0880	0.1416	0.7756
	A_T (L/mg)	1.58	2.09	52.17
	R^2	0.8623	0.8414	0.8853
Dubinin–Radushkevich	q_{DR} (mg/g)	1272.86	1395.19	1306.40
	K_{DR} (mol^2/kJ^2)	212.64	282.59	245.81
	E (kJ/mol)	0.0485	0.0421	0.0451
	R^2	0.9491	0.9073	0.9538
Sips	K_s (L/mg)	0.0001	4.6292×10^{-17}	1.1207×10^{-6}
	a_s (L/mg)	9.66×10^{-8}	4.32×10^{-20}	1.04×10^{-9}
	b_s	4.40	11.83	5.55
	R^2	0.9577	0.9904	0.9766

ATZ by the three adsorbents. The Sips model index (b_s) is related to the heterogeneity of the adsorption process (Álvarez et al., 2015; Dehghani et al., 2016; To et al., 2017), and the values for ATZ adsorption by GO, rGO and GNP were 4.40,

Table 5
Comparison of adsorption capacity for ATZ on different adsorbents.

Adsorbents	Adsorption capacity (mg/g)	Reference
Zr6-based metal–organic frameworks (MOFs)	36	Akpinar et al. (2019)
Activated carbon	92.23	Tan et al. (2016)
Apricot Kernel Shell Biochar	7.72	Zhang et al. (2022)
Modified montmorillonite	23.53	Park et al. (2014)
Activated carbon	104.9	Gupta et al. (2011)
MMWCNT	40.16	Tang et al. (2012)
Graphene Oxide (GO)	1011.94	
reduced Graphene Oxide (rGO)	1083.94	This work
Graphene nanoplatelets (GNP)	1005.77	

11.83 and 5.55, respectively, which are all much greater than 1, indicating that the adsorption is a heterogeneous process. Sips isotherm can be used to describe the adsorption of heterogeneous surfaces. The surface of these GBMs is composed of various functional groups such as COOH, OH and C–O–C, which may account for the heterogeneous process of ATZ adsorption and also why the Sips model has the best fitting (Yu et al., 2016).

3.5. Theoretical calculation and adsorption mechanism

To further investigate the adsorption mechanism of ATZ on GBMs, a computational simulation was implemented using DFT. It has been reported that the adsorption of GBMs for pollutants mainly depends on the sp^2 region and oxygen-containing functional groups (sp^3 region) in their own structure, in which the interaction mechanisms generally include hydrogen bonding and π–π conjugation (Huong et al., 2018). As presented in Table 3, the adsorption capacity of the GBMs for ATZ follows the order of rGO (1083.94 mg/g) > GO (1011.94 mg/g) > GNP (1005.77 mg/g). Some studies have reported that the key factors influencing the adsorption of adsorbate onto GBMs are the surface area, π–π conjugation and H-bonding (Foschi et al., 2021). Therefore, the adsorption capacity of GO, rGO and GNP is largely dependent on their own surface properties, such as oxygen-containing groups and the sp^2 region, which can greatly influence the H-bonding and π–π stacking interaction. To confirm the mechanisms for the adsorption behavior at the molecular level, the representative functional domains (sp^2 and sp^3 region) of GBMs were chosen and DFT was employed to calculate the interactions of ATZ with the sp^2 region [GBMs(sp^2)-ATZ] and sp^3 region of GBMs [GBMs(sp^3)-ATZ]. Fig. 5 presents the visual illustrations of the optimized structure and the colored isosurfaces for the investigated models. According to the optimized geometry of the sp^3 (Fig. 5a) and sp^2 region (Fig. 5b) of GBMs with ATZ, the interaction distance between GBMs and ATZ molecules was lower than 3.5 Å, illustrating that the interactions between GBMs and ATZ molecules are effective interactions. The interactions between ATZ molecules and the adsorbents were visualized through the isosurface of IGMH (isovalue = 0.005 a.u.) (Fig. 5c-d), which was mapped by sign (λ_2) ρ function. It is known that the surfaces with electron density $[\rho(r)] < 0.005$ a.u. are generally mapped into van der Waals (vdW) interactions (colored with green) and the surfaces with $0.005 < \rho(r) < 0.05$ a.u. are mapped into H-bonding (colored with blue) (Johnson et al., 2010). As shown in Fig. 5 (c-d), the interactions between ATZ and adsorbents could be clearly revealed by the color mapped isosurfaces. The isosurfaces of GBMs(sp^3)-ATZ are colored as blue and green, indicating that ATZ interacts with GBMs by both H-bonding and vdW interactions (Fig. 5c). However, in Fig. 5d, the isosurfaces of GBMs(sp^2)-ATZ are all marked as green, revealing that the interactions between ATZ and the sp^2 region of GBMs are vdW interactions, namely π–π stacking interactions. In the optimized geometry of the sp^3 region of GBMs with ATZ (Fig. 5a), the interaction distance between ATZ molecules and GBMs mainly by H-bonding was 1.76, 2.01 and 2.20 Å, respectively; while in GBMs(sp^2)-ATZ (Fig. 5b), the ATZ molecule interacts with GBMs(sp^2) by π–π stacking interaction with an interaction distance of 3.31 Å. The BE of GBMs(sp^3)-ATZ was 4.54 Kcal/mol lower than that of GBMs(sp^2)-ATZ, suggesting that the GBMs(sp^3)-ATZ structure is more stabilized. All these results suggested that the H-bonding interaction between ATZ and GBMs is stronger than the π–π stacking interaction, which is more conducive to the adsorption of adsorbate. This result is in accordance with the finding that compared with graphene, GO complexes are more stable due to the existence of H-bonding interactions (Vovusha et al., 2013). Therefore, GNP exhibited the lowest adsorption capacity for ATZ due to the few oxygen-containing groups, indicating that the adsorption of ATZ largely depends on the π–π stacking interaction. However, for GO and rGO, the adsorption might occur under the synergistic effect of H-bonding and π–π stacking interactions.

In addition, the isosurface of GBMs (sp^3 region) with ATZ implied that the H-bonding interactions of ATZ with GBMs mainly act on the bridging oxygen and hydroxyl oxygen groups, in which the carboxyl group plays a minor role (Fig. 5c). Compared with GO, rGO had more bridging oxygen and hydroxyl oxygen groups in the sp^3 region, which is more conducive to the adsorption of ATZ. This may be the reason for the highest adsorption capacity of rGO for ATZ among all absorbents, which is consistent with the experimental results. It can be thus concluded that in the adsorption process, ATZ interacts with the adsorbents through H-bonding and π–π stacking, which together promote the adsorption capacity (as shown in **Fig. S4**).
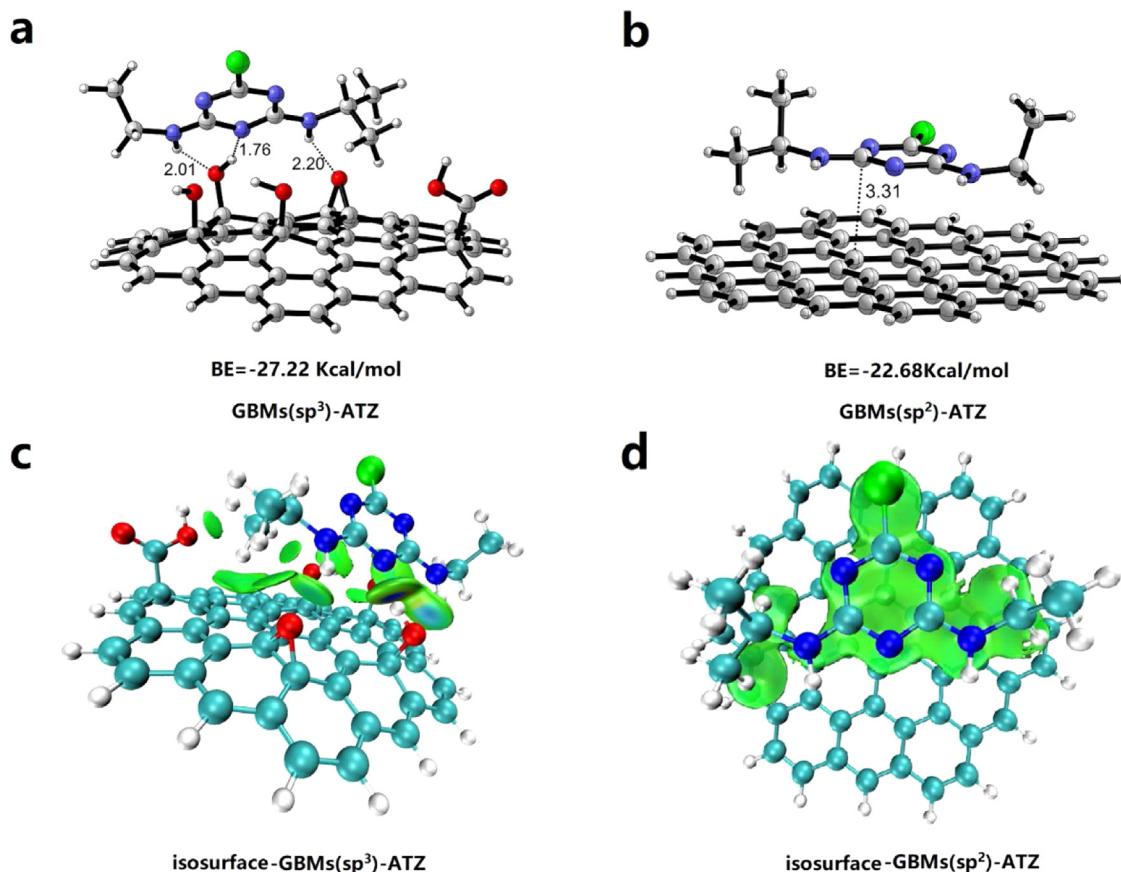
Fig. 5. Optimized geometry of the sp^3 and sp^2 region of GBMs with ATZ (bond lengths in Å) (a, b). Isosurface map for ATZ with isovalue = 0.005 a.u. onto the sp^3 region of GBMs [isosurface-GBM(sp^3)-ATZ] (c) and the sp^2 region of GBMs [isosurface-GBM(sp^2)-ATZ] (d) corresponding to IGMH analyses.

3.6. Real sample test

The application experiments of the three GBMs were carried out by adsorption of ATZ (100 mg/L) from tap water and wastewater to evaluate their applicability in actual samples. The adsorption capacities of GO, rGO and GNP for ATZ were 1078.24, 1150.36 and 1011.66 mg/g in tap water, and were 1086.49, 1142.84 and 975.52 mg/g in wastewater, respectively (**Fig. S5**). The results demonstrated that GO, rGO and GNP have extraordinary adsorption capacities for ATZ in tap water. Due to the presence of complex matrix, the adsorption capacity for ATZ in wastewater was slightly lower. Obviously, rGO has the highest adsorption capacity among the three materials, which may be ascribed to the interactions between the adsorbent and adsorbate as discussed in the previous section. The results suggest that the GBMs can be used for the removal of ATZ from the aqueous environment and provide important implications for the removal of pesticides from the environment in actual practice. However, compared with the three materials in the actual application process, GNP is more suitable for practical application due to its lower cost.

3.7. Reutilization test

In order to verify the recyclability of the adsorbents, recycling experiments were carried out. As shown in **Fig. S6**, GO, rGO and GNP were reused to adsorb ATZ. At the first repetition, GO, rGO and GNP maintained a high adsorption capacity for ATZ. The adsorption rate of GO, rGO and GNP was 98.2%, 98.7% and 97.5%, respectively. At the second repetition, the adsorption rate of GO, rGO and GNP for ATZ decreased by 2.6%, 2.1% and 4.2%, respectively, which still showed a good adsorption effect on ATZ. After the third repetition, the adsorption rate of GO, rGO and GNP for ATZ was still higher than 95%, indicating that the three adsorbents have good reusability. In addition, it is easy to operate the adsorbate elution by dichloromethane, which greatly facilitates the reutilization of adsorbents.

4. Conclusions

Three GBMs were used as absorbents for the removal of ATZ from aqueous solutions and characterized by SEM, TGA, XPS, FTIR and Raman spectroscopy. Experimental results revealed that all the three materials exhibited extraordinarily high adsorption capacity for ATZ with an order of rGO > GO > GNP. DFT was employed to study the interactions of ATZ with absorbents and give visual illustration by IGMH analyses, which can explain the sequence of adsorption capacity. The adsorption kinetic and adsorption isotherm fitting results demonstrated that the adsorption is a heterogeneous and multi-mechanism adsorption process, which can be attributed to the synergistic effect of H-bonding and $\pi-\pi$ conjugated interaction between ATZ and GBMs. The developed materials are inexpensive, convenient and feasible, and can be used to realize the removal of ATZ from the aqueous environment and provide reference for the adsorption of other pesticides in actual application.

CRediT authorship contribution statement

Caihong Cheng: Carried out the experiments, Proofread the references, Writing – original draft, Contributed substantially to the final text, tables, figure and discussed the results. **Xuejuan Shi:** Carried out the experiments, Analysis and interpretation of data, Writing – original draft, Contributed substantially to the final text, tables, figure and discussed the results. **Gengwen Yin:** Analysis and interpretation of data, Proofread the references, Contributed substantially to the final text, tables, figure and discussed the results. **Fei Peng:** Analysis and interpretation of data, Proofread the references, Contributed substantially to the final text, tables, figure and discussed the results. **Wenlong Hou:** Technical and material support, Contributed substantially to the final text, tables, figure and discussed the results. **Weiguo Zhang:** Technical and material support, Contributed substantially to the final text, tables, figure and discussed the results. **Xiaohu Lin:** Technical and material support, Contributed substantially to the final text, tables, figure and discussed the results. **Jun Li:** Revised the manuscript, Contributed substantially to the final text, tables, figure and discussed the results. **Xiuping Wang:** Conceived and designed the research, Revised the manuscript, Contributed substantially to the final text, tables, figure and discussed the results.

Declaration of competing interest

The authors declare that they have no known competing financial interests or personal relationships that could have appeared to influence the work reported in this paper.

Data availability

No data was used for the research described in the article.

Acknowledgment

Appendix A. Supplementary data

Supplementary material related to this article can be found online at https://doi.org/10.1016/j.eti.2022.102823.

References

Adeniyi, AG., Igwegbe, CA., Ighalo, JO., 2021. ANN Modelling of the adsorption of herbicides and pesticides based on Sorbate-Sorbent interphase. Chem. Afr. http://dx.doi.org/10.1007/s42250-020-00220-w.

Akpinar, I., Drout, RJ., Islamoglu, T., Kato, S., Lyu, J., Farha, OK., 2019. Exploiting $\pi--\pi$ interactions to design an efficient sorbent for Atrazine removal from water. JACS Appl. Mater. Interfaces 11, 6097–6103. http://dx.doi.org/10.1021/acsami.8b20355.

Al-Ghouti, MA., Sayma, J., Munira, N., Mohamed, D., Da'na, DA., Qiblawey, H., Alkhouzaam, A., 2022. Effective removal of phenol from wastewater using a hybrid process of graphene oxide adsorption and UV-irradiation. Environ. Technol. Innov. 27, 102525. http://dx.doi.org/10.1016/j.eti.2022.102525.

Álvarez, S., Ribeiro, RS., Gomes, HT., Sotelo, JL., García, J., 2015. Synthesis of carbon xerogels and their application in adsorption studies of caffeine and diclofenac as emerging contaminants. Chem. Eng. Res. Des. 95, 229–238. http://dx.doi.org/10.1016/j.cherd.2014.11.001.

Banisheykholeslami, F., Hosseini, M., Darzi, G.N., 2021. Design of PAMAM grafted chitosan dendrimers biosorbent for removal of anionic dyes: Adsorption isotherms, kinetics and thermodynamics studies. Int. J. Biol. Macromol. 177, 306–316. http://dx.doi.org/10.1016/j.ijbiomac.2021.02.118.

Bhattacharyya, A., Ghorai, S., Chattopadhyay, D., Roy, I., Sarkar, G., Saha, NR., Orasugh, J.T., De, S., Sadhukhan, S., Chattopadhyay, D., 2021. Design of an efficient and selective adsorbent of cationic dye through activated carbon-graphene oxide nanocomposite: study on mechanism and synergy. Mater. Chem. Phys. 260, 124090. http://dx.doi.org/10.1016/j.matchemphys.2020.124090.

Binh, QA., Nguyen, VH., Kajitvichyanukul, P., 2022. Influence of pyrolysis conditions of modified corn cob bio-waste sorbents on adsorption mechanism of atrazine in contaminated water. Environ. Technol. Innov. 28, 102595. http://dx.doi.org/10.1016/j.eti.2022.102381.

Dehghani, MH., Mohammadi, M., Mohammadi, MA., Mahvi, AH., Yetilmezsoy, K., Bhatnagar, A., Heibati, B., McKay, G., 2016. Equilibrium, kinetic studies of trihalomethanes adsorption onto multi-walled carbon nanotubes. Water Air Soil Pollut. 227, 332. http://dx.doi.org/10.1007/s11270-016-3029-2.

Dionne, E., Hanson, ML., Anderson, JC., Brain, RA., 2021. Chronic toxicity of technical atrazine to the fathead minnow (*Pimephales promelas*) during a full life-cycle exposure and an evaluation of the consistency of responses. Sci. Total Environ. 755, 142589. http://dx.doi.org/10.1016/j.scitotenv.2020.142589.

El-Kammah, M., Elkhatib, E., Gouveia, S., Cameselle, C., Aboukila, E., 2022. Cost-effective ecofriendly nanoparticles for rapid and efficient indigo carmine dye removal from wastewater: Adsorption equilibrium, kinetics and mechanism. Environ. Technol. Innov. 28, 102595. http://dx.doi.org/10.1016/j.eti.2022.102595.

Fareed, A., Hussain, A., Nawaz, M., Imran, M., Ali, Z., Haq, SU., 2021. The impact of prolonged use and oxidative degradation of Atrazine by fenton and photo-Fenton processes. Environ. Technol. Innov. 24, 101840. http://dx.doi.org/10.1016/j.eti.2021.101840.

Foschi, M., Capasso, P., Maggi, MA., Ruggieri, F., 2021. Experimental design and response surface methodology applied to graphene oxide reduction for adsorption of Triazine herbicides. ACS Omega 6, 16943–16954. http://dx.doi.org/10.1021/acsomega.1c01877.

Gao, Y., Su, K.M., Li, Z.H., Cheng, B.W., 2018. Graphene oxide hybrid poly(p-phenylene sulfide) nanofiltration membrane intercalated by bis(triethoxysilyl) ethane. Chem. Eng. J. 352, 10–19. http://dx.doi.org/10.1016/j.cej.2018.06.180.

Grimme, S., Ehrlich, S., Goerigk, L., 2011. Effect of the damping function in dispersion corrected density functional theory. J. Comput. Chem. 32, 1456–1465. http://dx.doi.org/10.1002/jcc.21759.

Gupta, VK., Gupta, B., Rastogi, A., Agarwal, S., Nayak, A., 2011. Pesticides removal from waste water by activated carbon prepared from waste rubber tire. Water Res. 45, 4047–4055. http://dx.doi.org/10.1016/j.watres.2011.05.016.

Hamilton, PB., Lavoie, I., Ley, LM., Poulin, M., 2011. Factors contributing to the spatial and temporal variability of phytoplankton communities in the Rideau River (Ontario, Canada). River Syst. 19, 189–205. http://dx.doi.org/10.1127/1868-5749/2011/019-0026.

He, H., Liu, Y., You, S., Liu, J., Xiao, H., Tu, Z., 2019. A review on recent treatment technology for herbicide atrazine in contaminated environment. Int. J. Environ. Res. Public Health 16 (5129), http://dx.doi.org/10.3390/ijerph16245129.

Huang, F., Zhang, L., Wu, RR., Zhang, SM., Xiao, RB., 2020. Adsorption behavior and relative distribution of Cd^{2+} adsorption mechanisms by the magnetic and nonmagnetic biochars derived from chicken manure. Int. J. Environ. Res. Public Health 17 (1602), http://dx.doi.org/10.3390/ijerph17051602.

Huong, P., Tu, N., Lan, H., Thang, LH., Quy, NV., Tuan, PA., Dinh, NX., Phan, VN., Le, AT., 2018. Functional manganese ferrite/graphene oxide nanocomposites: effects of graphene oxide on the adsorption mechanisms of organic MB dye and inorganic As(V) ions from aqueous solution. Rsc Adv. 8, 12376–12389. http://dx.doi.org/10.1039/c8ra00270c.

Ighalo, JO., Adeniyi, AG., Adelodun, AA., 2020. Recent advances on the adsorption of herbicides and pesticides from polluted waters: performance evaluation via physical attributes. J. Ind. Eng. Chem. http://dx.doi.org/10.1016/j.jiec.2020.10.011.

Isiuku, BO., Okonkwo, PC., Emeagwara, CD., 2021. Batch adsorption isotherm models applied in single and multicomponent adsorption systems - a review. J. Dispers. Sci. Technol. 42, 1879–1897. http://dx.doi.org/10.1080/01932691.2021.1964988.

Johnson, ER., Keinan, S., Mori-Sánchez, P., Contreras-García, J., Cohen, AJ., Yang, W., 2010. Revealing noncovalent interactions. J. Am. Chem. Soc. 132, 6498–6506. http://dx.doi.org/10.1021/ja100936w.

Kesarwani, H., Saxena, A., Mandal, A., Sharma, S., 2021. Anionic/nonionic surfactant mixture for enhanced oil recovery through the investigation of adsorption, interfacial, rheological, and rock wetting characteristics. Energy Fuels 35, 3065–3078. http://dx.doi.org/10.1021/acs.energyfuels.0c03767.

Khavar, AHC., Moussavi, G., Mahjoub, AR., Satari, M., Abdolmaleki, P., 2018. Synthesis and visible-light photocatalytic activity of In, S-TiO2@rGO nanocomposite for degradation and detoxification of pesticide atrazine in water. Chem. Eng. J. 345, 300–311. http://dx.doi.org/10.1016/j.cej.2018.03.095.

Kong, X., Jiang, J., Ma, J., Yang, Y., Liu, W., Liu, Y., 2016. Degradation of atrazine by UV/chlorine: efficiency, influencing factors, and products. Water Res. 90, 15–23. http://dx.doi.org/10.1016/j.watres.2015.11.068.

Kuang, Y., Zhang, XP., Zhou, SQ., 2020. Adsorption of methylene blue in water onto activated carbon by surfactant modifification. Water 12 (587), http://dx.doi.org/10.3390/w12020587.

Li, B., Chen, XW., Zhang, TY., Jiang, S., Zhang, GH., Wu, WB., Ma, XY., 2018. Photocatalytic selective hydroxylation of phenol to dihydroxybenzene by BiOI/TiO2 p-n heterojunction photocatalysts for enhanced photocatalytic activity. Appl. Surf. Sci. 439, 1047–1056. http://dx.doi.org/10.1016/j.apsusc.2017.12.220.

Li, H., Wang, F., Li, J., Deng, S., Zhang, S., 2021. Adsorption of three pesticides on polyethylene microplastics in aqueous solutions: Kinetics, isotherms, thermodynamics, and molecular dynamics simulation. Chemosphere 264, 128556. http://dx.doi.org/10.1016/j.chemosphere.2020.128556.

Liu, G., Wang, Y.J., Wang, X.J., Jiang, Y., Cheng, L.L., Jiao, Z., 2015. One-step synthesis of high conductivity silver nanoparticle-reduced graphene oxide composite films by electron beam irradiation. Appl. Surf. Sci. 349, 570–575. http://dx.doi.org/10.1016/j.apsusc.2015.05.044.

Lu, T., Chen, FW., 2012. Multiwfn: A multifunctional wavefunction analyzer. J. Comput. Chem. 33, 580–592. http://dx.doi.org/10.1002/jcc.22885.

Lu, T., Chen, QX., 2021. Independent gradient model based on hirshfeld partition (IGMH): A new method for visual study of interactions in chemical systems. ChemRxiv http://dx.doi.org/10.26434/chemrxiv-2021-628vh-v2.

Mclean, AD., Chandler, GS., 1980. Contracted gaussian basis sets for molecular calculations. i. second row atoms, z=11-18. J. Chem. Phys. 72, 5639–5648. http://dx.doi.org/10.1063/1.438980.

Mehrabi, N., Masud, A., Afolabi, M., Hwang, J., Ortiz, GAC., Aich, N., 2019. Magnetic graphene oxide-nano zero valent iron (GO-nZVI) nanohybrids synthesized using biocompatible cross-linkers for methylene blue removal. RSC Adv. 9, 963–973. http://dx.doi.org/10.1039/C8RA08386J.

Molla, A., Li, YY., Mandal, B., Kang, SG., Hur, SH., Chung, JS., 2019. Selective adsorption of organic dyes on graphene oxide: Theoretical and experimental analysis. Appl. Surf. Sci. 464, 170–177. http://dx.doi.org/10.1016/j.apsusc.2018.09.056.

Nithya Priya, V., Rajkumar, M., Mobika, J., Lint Sibi, SP., 2022. Adsorption of As(V) ions from aqueous solution by carboxymethyl cellulose incorporated layered double hydroxide/reduced graphene oxide nanocomposites: Isotherm and kinetic studies. Environ. Technol. Innov. 26, 102268. http://dx.doi.org/10.1016/j.eti.2022.102268, 022.

Nodeh, HR., Kamboh, A., Ibrahim, W., Jume, BH., Sereshti, H., Sanagi, MM., 2019. Equilibrium, kinetic and thermodynamic study of pesticides removal from water using novel glucamine-calix[4]arene functionalized magnetic graphene oxide. Environ. Sci.: Process. Impacts 21, 714–726. http://dx.doi.org/10.1039/C8EM00530C.

Park, Y., Sun, Z., Ayoko, GA., Frost, RL., 2014. Removal of herbicides from aqueous solutions by modified forms of montmorillonite. J. Colloid Interface Sci. 415, 127–132. http://dx.doi.org/10.1016/j.jcis.2013.10.024.

Saxena, N., Kumar, A., Mandal, A., 2019. Adsorption analysis of natural anionic surfactant for enhanced oil recovery: The role of mineralogy, salinity, alkalinity and nanoparticles. J. Pet. Sci. Eng. 173, 1264–1283. http://dx.doi.org/10.1016/j.petrol.2018.11.002.

Souza, RMD., Seibert, D., Quesada, HB., Bassetti, FDJ., Fagundes-Klen, MR., Bergamasco, R., 2020. Occurrence, impacts and general aspects of pesticides in surface water: A review. Process Saf. Environ. Prot. 135, 22–37. http://dx.doi.org/10.1016/j.psep.2019.12.035.

Srivastava, V., Shekhar, M., Gusain, D., Gode, F., Sharma, YC., 2017. Application of a heterogeneous adsorbent (HA) for the removal of hexavalent chromium from aqueous solutions: Kinetic and equilibrium modeling. Arab. J. Chem. 10, S3073–S3083. http://dx.doi.org/10.1016/j.arabjc.2013.11.049.

Sui, D., Li, H., Chai, Y., Li, J., Liu, S., Zhao, Y., Fan, H., Xu, H., 2017. Adsorption characteristics of tetracycline antibiotics from aqueous solution onto graphene nanoplatelets: Equilibrium, kinetic and thermodynamic studies. Desalin. Water Treat. 94, 263–271. http://dx.doi.org/10.5004/dwt.2017.21597.

Tan, G., Xu, N., Xu, Y., Wang, H., Sun, W., 2016. Sorption of mercury (II) and atrazine by biochar, modified biochars and biochar based activated carbon in aqueous solution. Bioresour. Technol. 211, 727–735. http://dx.doi.org/10.1016/j.biortech.2016.03.147.

Tang, W., Zeng, G., Gong, J., Liu, Y., Wang, X., Liu, Y., Liu, Z., Chen, L., Zhang, X., Tu, D., 2012. Simultaneous adsorption of atrazine and Cu(II) from wastewater by magnetic multi-walled carbon nanotube. Chem. Eng. J. 211–212, 470–478. http://dx.doi.org/10.1016/j.cej.2012.09.102.

To, MH., Hadi, P., Hui, CW., Lin, CSK., McKay, G., 2017. Mechanistic study of atenolol: acebutolol and carbamazepine adsorption on waste biomass derived activated carbon. J. Molecular Liquids 241, 386–398. http://dx.doi.org/10.1016/j.molliq.2017.05.037.

Tran, HN., You, SJ., Hosseini-Bandegharaei, A., Chao, H.P., 2017. Mistakes and inconsistencies regarding adsorption of contaminants from aqueous solutions: a critical review. Water Res. 120, 88–116. http://dx.doi.org/10.1016/j.watres.2017.09.055.

Velásquez-Rojas, MM., Contreras-Torres, FF., Meza-Laguna, V., Álvarez-Zauco, E., Farías, MH., Basiuk, VA., Basiuk, EV., 2021. Solvent-free functionalization of graphene oxide powder and paper with aminobenzo-crown ethers and complexation with alkali metal cations. Mater. Chem. Phys. 260, 124127. http://dx.doi.org/10.1016/j.matchemphys.2020.124127.

Vieira, LAJ., Alves, RDFB., Menezes-Silva, PE., Mendonça, MLF., Silva, MAC., Silva, MCAP., Sousa, LF., Loram-Lourenço, L., Silva, AA., Costa, AC., Silva, FG., Farnese, FS, 2021. Water contamination with atrazine: is nitric oxide able to improve pistia stratiotes phytoremediation capacity? Environ. Pollut. 272, 115971. http://dx.doi.org/10.1016/j.envpol.2020.115971.

Vovusha, V., Sanyal, S., Vovusha, B., 2013. Interaction of nucleobases and aromatic amino acids with graphene oxide and graphene flakes. J. Phys. Chem. Lett. 4, 3710–3718. http://dx.doi.org/10.1021/jz401929h.

Wang, PP., Liu, XG., Yu, BC., Wu, XH., Xu, J., Dong, FS., Zheng, YQ., 2020. Characterization of peanut-shell biochar and the mechanisms underlying its sorption for atrazine and nicosulfuron in aqueous solution. Sci. Total Environ. 702, 134767. http://dx.doi.org/10.1016/j.scitotenv.2019.134767.

Wang, RH., Wang, Y., Xu, CH., Sun, J., Gao, L., 2013. Facile one-step hydrazine-assisted solvothermal synthesis of nitrogen-doped reduced graphene oxide: reduction effect and mechanisms. RSC Adv. 3, 1194–1200. http://dx.doi.org/10.1039/C2RA21825A.

Wang, X., Xie, H., Wang, Z., He, K., Jing, D., 2018. Graphene oxide as a multifunctional synergist of insecticides against lepidopteran insect. Environ. Sci.: Nano 6, 75–84. http://dx.doi.org/10.1039/c8en00902c.

Wanjeria, VWO., Sheppard, CJ., Prinsloo, ARE., Ngila, JC., Ndungu, PG., 2018. Isotherm and kinetic investigations on the adsorption of organophosphorus pesticides on graphene oxide based silica coated magnetic nanoparticles functionalized with 2-phenylethylamine. J. Environ. Chem. Eng. 6, 1333–1346. http://dx.doi.org/10.1016/j.jece.2018.01.064.

Yang, L., Li, H., Zhang, Y., Jiao, N., 2019. Environmental risk assessment of triazine herbicides in the Bohai Sea and the Yellow Sea and their toxicity to phytoplankton at environmental concentrations. Environ. Int. 133, 105175. http://dx.doi.org/10.1016/j.envint.2019.105175.

Yang, Z., Yu, A., Shan, C., Gao, G., Pan, B., 2018. Enhanced Fe(III)-mediated fenton oxidation of atrazine in the presence of functionalized multi-walled carbon nanotubes. Water Res. 137, 37–46. http://dx.doi.org/10.1016/j.watres.2018.03.006.

Yu, SJ., Wang, XX., Ai, YJ., Tan, XL., Haya, T., Hu, WP., Wang, XK., 2016. Experimental and theoretical study on competitive adsorption of aromatic compounds on reduced graphene oxides. J. Mater. Chem. A 6, 19–40. http://dx.doi.org/10.1039/C6TA00890A.

Yu, XR., Zhang, RR., Liu, H., Zhang, ZM., Shi, XZ., Sun, AL., Chen, J., 2021. Highly-selective complex matrices removal via a modified QuEChERS for determination of triazine herbicide residues and risk assessment in bivalves. Food Chem. 347, 129030. http://dx.doi.org/10.1016/j.foodchem.2021.129030.

Yuan, X., Xie, R., Zhang, Q., Sun, L., Long, X., Xia, D., 2019. Oxygen functionalized graphitic carbon nitride as an efficient metal-free ozonation catalyst for atrazine removal: performance and mechanism. Sep. Purif. Technol. 211, 823–831. http://dx.doi.org/10.1016/j.seppur.2018.10.052.

Zarenezhad, M., Zarei, M., Ebratkhahan, M., Hosseinzadeh, M., 2022. Synthesis and study of functionalized magnetic graphene oxide for Pb2+ removal from wastewater. Environ. Technol. Innov. 22, 101384. http://dx.doi.org/10.1016/j.eti.2021.101384.

Zhang, Z., Zhou, C., Yang, J., Yan, B., Liu, J., Wang, S., Li, Q., Zhou, M., 2022. Preparation and characterization of apricot kernel shell biochar and its adsorption mechanism for atrazine. Sustainability 14 (4082), http://dx.doi.org/10.3390/su14074082.

Zhao, CQ., Hong, PD., Li, YJ., Song, XM., Wang, YG., Yang, YS., 2019. Mechanism of adsorption of tetracycline-cu multi-pollutants by graphene oxide (GO) and reduced graphene oxide (rGO). J. Chem. Technol. Biotechnol. 94, 1176–1186. http://dx.doi.org/10.1002/jctb.5864.

Zhao, Y., Schultz, NE., Truhlar, DG., 2006. Design of density functionals by combining the method of constraint satisfaction with parametrization for thermochemistry, thermochemical kinetics, and noncovalent interactions. J. Chem. Theory Comput. 2, 364–382. http://dx.doi.org/10.1021/ct0502763.